Research Square

Preprints are preliminary reports that have not undergone peer review.
They should not be considered conclusive, used to inform clinical practice,
or referenced by the media as validated information.

Role of Spatial and Temporal Pulse Delivery in the Formation of Self- Organized Surface Structures during Picosecond Laser Structuring of Stainless Steel

Yasmine Bouraoui
BIAS – Bremer Institut für angewandte Strahltechnik GmbH
Peer Woizeschke
BIAS – Bremer Institut für angewandte Strahltechnik GmbH
Tim Radel
radel@bias.de

BIAS – Bremer Institut für angewandte Strahltechnik GmbH

Research Article

Keywords:

Posted Date: November 23rd, 2026

DOI: https://doi.org/10.21203/rs.3.rs-11649933/v1

License: This work is licensed under a Creative Commons Attribution 4.0 International License.
Read Full License

Additional Declarations: No competing interests reported.

Role of Spatial and Temporal Pulse Delivery in the Formation of Self-Organized Surface Structures during Picosecond Laser Structuring of Stainless Steel

Bouraoui, Y. [a]; Woizeschke, P.[a b]; Radel, T.[* a b]

[a]BIAS – Bremer Institut für angewandte Strahltechnik GmbH, Klagenfurter Straße 5, Bremen, 28359

[b]MAPEX Center for Materials and Processes – University of Bremen, Bibliothekstraße 1, 28359 Bremen, Germany

*Corresponding author. Tel.: +49 421 218 58089; e-mail address: radel@bias.de

Abstract

Self-organized surface structures were generated on AISI 304 stainless steel (X5CrNi18-10) by picosecond laser scanning to investigate the combined influence of peak fluence, accumulated spatial exposure, and temporal pulse delivery on the formation of grooves and spikes. The resulting morphologies were classified using scanning electron microscopy and two-dimensional fast Fourier transform (2D-FFT) analysis and their characteristic spatial periods, formation mechanisms and achievable structuring rates were evaluated. The morphology maps show that peak fluence and the effective number of pulses determine the main progression from grooves to mixed structures and spikes, while repetition rate additionally influences this evolution. Comparable spatial irradiation conditions at 50 kHz and 100 kHz resulted in different morphologies and structural dimensions, demonstrating that accumulated spatial exposure alone does not fully describe the structuring process. Lower repetition rates promoted an earlier transition toward grooves and generally resulted in larger spikes, whereas grooves showed weaker sensitivity to repetition rate. At the highest investigated peak fluence, inhomogeneous and chaotic textures were obtained. Cross-sectional observations showed that the structures remained below the initial surface level, supporting preferential valley ablation as a possible dominant spikes formation mechanism. The achievable structuring rate depended on morphology, with grooves obtained at higher rates and increasing repetition rate shifting spikes formation toward higher processing rates.

1. Introduction

Surface physical and chemical properties of engineering materials strongly influence their interaction with the surrounding environment and, consequently, their functional performance [1]. Tailoring these properties enables the development of specific surface functionalities for optical, wetting and liquid-management [2], tribological [3], and biological applications [4]. One promising approach for creating such functionalities is surface structuring. Laser-based methods are particularly attractive because they enable localized surface modification with high precision and flexibility, for example by direct ablation using single or multiple beams. In addition to directly written geometries, ultrashort-pulse irradiation can generate self-organized structures with characteristic dimensions and spatial organization depending on the laser-material interaction [1]. The formation of these structures is not limited to a specific class of material but represents a universal phenomenon. Self-organized surface structures have been observed on conductive metals and semiconductors [5], dielectrics [6] and polymers [7].

Self-organized morphologies include laser-induced periodic surface structures (LIPSS), grooves, and spikes. LIPSS are low-spatial-frequency LIPSS (LSFL) with periods of the order of the laser

wavelength, while high-spatial-frequency LIPSS (HSFL) have significantly smaller periods. On metals, LSFL are commonly oriented perpendicular to the polarization direction of linearly polarized irradiation. Grooves are quasi-periodic structures with characteristic dimensions of a few micrometers and orientation parallel to polarization, whereas spikes exhibit larger characteristic dimensions and generally show a weaker correlation with the polarization direction. Grooves are usually described as an intermediate morphology between LIPSS and spikes [8].

The resulting morphology depends on the laser parameters, irradiation history, and material properties. Relevant processing parameters include wavelength, pulse duration, polarization, fluence, and the number of pulses irradiating a surface location. During scanning, pulse and line overlap determine the accumulated spatial exposure. Increasing the accumulated pulse exposure can promote a progressive evolution from nanoscale LIPSS toward larger grooves and spikes [9] The corresponding formation and transition conditions depend on the applied fluence and material response [10]. Multi-pulse irradiation is additionally affected by incubation effects, whereby the fluence threshold required for the formation of a given laser-induced structure decreases with increasing pulse number at the same location. Therefore, the incubation effect implies that the material response is altered during repeated irradiation. In scanning processes, increasing pulse-to-pulse and line overlap increases the effective number of pulses incident on a given location and can subsequently reduce the fluence threshold for the formation of a particular structure. These formation conditions are strongly material dependent and different morphologies may consequently occur on different materials under similar irradiation conditions [10]. However, accumulated spatial exposure and temporal pulse delivery represent distinct aspects of the irradiation history [11]. Spatial accumulation is determined by the successive pulse positions along the scanning direction together with the overlap of neighboring scan lines [12], whereas repetition rate determines the temporal separation between successive pulses [13]. As a result, heat accumulation can additionally impact the material response when the energy deposited has not sufficiently dissipated before subsequent irradiation [14]. In addition, several studies have addressed the mechanisms underlying the formation of self-organized structures and their subsequent evolution. LSFL-LIPSS formation on metals is generally attributed to a periodic modulation of the absorbed energy resulting from interference between the incident laser radiation and an excited or scattered electromagnetic surface wave. The resulting periodic energy deposition is transferred into the surface topography through repeated irradiation. Therefore, their characteristic period remains closely related to the laser wavelength and their orientation is strongly dependent on the laser polarization [15]. Compared to LIPSS, the origin of grooves remains less established. However, few studies related their formation to a transition from predominantly electromagnetic nanoscale organization toward a stronger contribution of material redistribution and hydrodynamic effects. In general, their occurrence was observed after a larger number of pulses or at increased irradiation levels and had periods exceeding the laser wavelength. Their development was then attributed to the progressive evolution of the preceding LSFL topography, which modifies the local electromagnetic energy deposition, but hydrodynamic processes in the transient molten layer become increasingly important. Hydrodynamic models based on Marangoni convection have been proposed to contribute to the development of larger-scale periodic grooves [16]. They typically form perpendicular to the LSFL and parallel to the laser polarization [15]. Spikes correspond to a further development toward three-dimensional microscale topography. Hydrodynamic models describe the transition from grooves to spikes through increasingly complex melt flow driven by temperature gradients, surface tension variations

and hydrothermal convection [17]. For metals, preferential ablation mechanisms were also reported. Zuhlke et al. distinguished below-surface growth (BSG), in which the structures remain below the original surface and develop predominantly through preferential removal of the surrounding material, from above-surface growth (ASG), in which material extends above the original surface and growth is dominated by melt flow and redeposition of ablated material. Both contributions may occur simultaneously, with one mechanism becoming dominant depending on the irradiation conditions [18]. Kam et al. further distinguished a near-threshold regime, in which isolated spikes nucleate from recondensed oxide-rich precursor particles, from a high-fluence regime characterized by initial surface roughening, local variations in absorption, and the simultaneous development of semi-regular spikes arrays [19].

Despite the extensive work on self-organized surface structuring, the interplay between peak fluence, accumulated spatial exposure, and temporal pulse delivery during picosecond raster scanning has not been systematically resolved for the transition between grooves and spikes. Comparable accumulated spatial exposure can be generated using different combinations of processing parameters while the temporal separation between successive pulses remains different. How this difference in pulse delivery affects the resulting morphology, the transition between grooves and spikes, and their characteristic spatial dimensions therefore requires further investigation. In addition, the gradual transition between self-organized morphologies can make their classification ambiguous, while the dominant formation mechanisms depend on the material and irradiation conditions. While the formation of self-organized micro- and nanostructures has been extensively investigated using femtosecond irradiation, picosecond processing has received comparatively less attention. However, similar self-organized structures can also be generated in the picosecond regime, which additionally offers economic benefits for laser processing [13]. In this work, the formation of self-organized surface structures on stainless steel AISI 304 is systematically investigated using 6 ps laser pulses. The combined influence of peak fluence F_0, effective two-dimensional pulse number $N_{eff,2D}$, and repetition rate on the resulting morphology and characteristic spatial dimensions is examined. Particular attention is given to the influence of temporal pulse delivery in relation to accumulated spatial exposure. The classification of the resulting morphologies and their transitions is further refined, and possible formation mechanisms under the investigated material and processing conditions are discussed. Finally, the identified morphology regimes are related to the achievable areal structuring rate, including the use of beam defocusing as a strategy for increasing the processed area.

2. Materials and Methods

2.1 Laser structuring and material

Surface structuring was conducted using a TruMicro 5050 (Yb:YAG) from TRUMPF laser system with a wavelength of 1030 nm, a pulse duration of 6 ps, pulse energies up to 250 µJ at a maximum repetition rate of 200 kHz. The laser delivers a linearly polarized Gaussian beam with a $1/e^2$ waist diameter of 46 µm. The beam was focused onto the sample surface using a Sill Optics f-theta lens with a focal length of 80 mm and beam scanning was performed by the hurrySCAN II 14 galvanometer scanner from SCANLAB GmbH.

The pulse energy E_p was maintained at 250 µJ, while the peak fluence was varied by changing the beam diameter through defocusing. Additional beam diameters of 55 µm and 115 µm were

obtained by positioning the sample surface at defocus distances of +2 mm and +4 mm, respectively. The peak fluence was calculated for a Gaussian beam according to:

$$F_0 = \frac{2 * E_p}{\pi * w^2} \quad (1)$$

Where E_p is the pulse energy and w is the beam radius at the respective z position.

Areal structuring was performed by scanning parallel lines across the sample surface. The scan velocity was increased from 150 mm/s up to 550 mm/s in 50 mm/s steps for repetition rates of 50 kHz and 100 kHz. The line distance was adjusted for each beam diameter to maintain a constant line overlap of 95%, corresponding to a line distance $h = 0.05 * d$. The combined spatial pulse accumulation resulting from the overlap of successive pulses in the scanning direction and neighboring lines was defined in [20] by the effective two-dimensional pulse number as:

$$N_{eff,2D} = \frac{\pi * w^2 * f}{v \cdot h} \quad (2)$$

Where f is the pulse repetition rate, v is the scan velocity, and h is the distance between adjacent scan lines. The areal structuring rate was calculated as $h * v$. Figure 1 schematically illustrates the experimental setup and scanning strategy. The processing parameters investigated are summarized in Table 1.

Table 1: Summary of process parameters used for surface structuring

Beam diameter d	Peak fluence F_0	Repetition rate f	Scan velocity v	Line distance h
µm	J/cm²	kHz	mm/s	µm
46 (z =0)	30.1	50;100	150 to 550	2.30
55 (z = +2)	21.1	50; 100	150 to 500	2.75
115 (z = +4)	4.8	50; 100	150 to 500	5.75

Austenitic stainless steel AISI 304 (1.4301/ X5CrNi18-10) samples were used. Due to its excellent corrosion resistance and high-temperature performance, it is one of the most widely used austenitic stainless steels in the food, chemical, aerospace, and automotive industries [21]. The initial areal surface roughness was Sa = 25 ± 5.8 nm. Before and after laser processing, the specimens were cleaned in an ultrasonic bath using isopropanol.

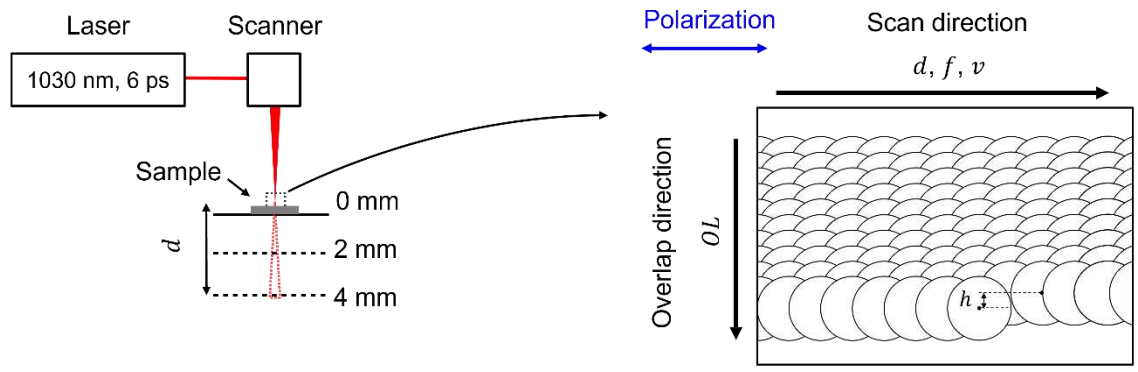

Figure 1: Schematic illustration of the experimental setup and detailed scanning strategy for picosecond surface structuring of AISI 304. The laser polarization is oriented parallel to the scanning direction and h represents the line distance in overlap direction OL corresponding to $h = 0.05 * d$.

The process parameters investigated resulted in nine matched F_0 vs. $N_{eff,2D}$ pairs with different repetition rates. These matched conditions were further investigated regarding the influence of repetition rate. The corresponding scan velocity pairs 500/250 mm/s, 400/200 mm/s and 300/150 mm/s at 100/50 kHz correspond to pulse-to-pulse displacements v/f of 5 µm, 4 µm and 3 µm, respectively. The temporal separation changes from 10 µs at 100 kHz to 20 µs at 50 kHz. For the matched conditions, a relative difference threshold of 15% was used to classify the characteristic spatial periods as comparable or different. Pairs with a relative difference of 15% or less were considered comparable, while values above 15% were classified as different. If the two samples belonged to different morphology classes, they were also classified as different.

2.2 Surface characterization

Surface morphologies were characterized using an EVO MA10 scanning electron microscope (Zeiss). The SEM images were additionally analyzed using a 2D-FFT-based classification script. The script allows systematic classification of the different morphologies and determination of their characteristic spatial periods. For spikes and grooves, the spatial periods were determined along their short axes due to the elongated and intermittent shapes observed in some textures. This direction corresponds to the established orientation of grooves parallel to the laser polarization and of the short axis of spikes parallel to the polarization. The spatial period along the long axis of spikes was not determined.

The classification follows a two-stage workflow to assign a primary morphology label and an additional dominance label for transition and mixed textures, see Figure 2. In the first stage, the two-dimensional power spectral density (PSD) resolves spatial-frequency content by power, direction and radius. Within the low-spatial-frequency band (wavenumbers below the laser wave vector k_λ), where grooves and spikes are expected to contribute, three angular sectors were defined relative to a fixed LIPSS reference orientation: LIPSS direction, grooves direction (orthogonal to LIPSS) and background for spikes, following the spectral distribution representation in [20]. Primary classification uses the ratio of the grooves power density to the background power density. Ratios above an empirically determined threshold are classified as grooves, whereas ratios below the threshold are classified as spikes. Because this ratio compresses a continuous, two-dimensional power distribution into one binary threshold, a secondary dominance label was

computed to identify samples in which a specific structural signal remains locally dominant or samples in which signals are comparable. In contrast to the classification ratio, which always compares grooves power density to background power density, the dominance compares only the two densities that are physically meaningful given the sample's primary classification, including LIPSS density. The classification script package is available in Mendeley Data [22].

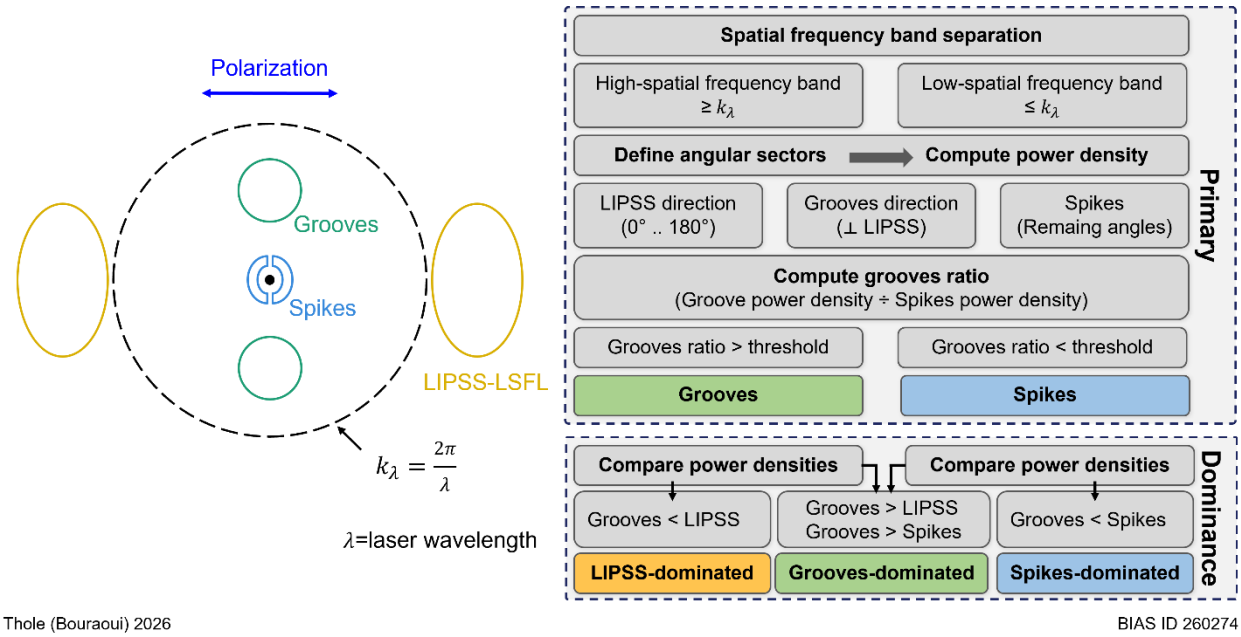

Figure 2: Classification of self-organized surface structures based on their quantitative spectral distribution in Fourier space relative to laser wave vector k_λ (black dashed circle) and orientation to laser polarization.

Cross sections were prepared from selected structured surfaces obtained at different peak fluences, repetition rates and scan velocities to support the assessment of possible formation mechanisms.

3. Results

Figure 3 shows representative SEM images of selected surface morphologies obtained at 100 kHz for the three investigated peak fluence levels and different scan velocities. At the highest peak fluence of 30.1 J/cm², the selected images show a change from chaotic textures, see Figure 3.a-b, to inhomogeneous structures with increasing scan velocity, Figure 3.c-d. The inhomogeneous surfaces exhibit pronounced spikes whose spatial distribution and shape vary across the processed area. In Figure 3.d, defined grooves clusters and spikes clusters are clearly visible. At 21.1 J/cm², the surface shows well-developed spikes with elongated and non-uniform spikes at lower scan velocities, see Figure 3.e and more uniform, rounded spikes toward higher scan velocities, see Figure 3.f-h. At 4.8 J/cm², spikes, grooves and mixed grooves-spikes textures occur depending on the processing condition, see Figure 3.i-l.

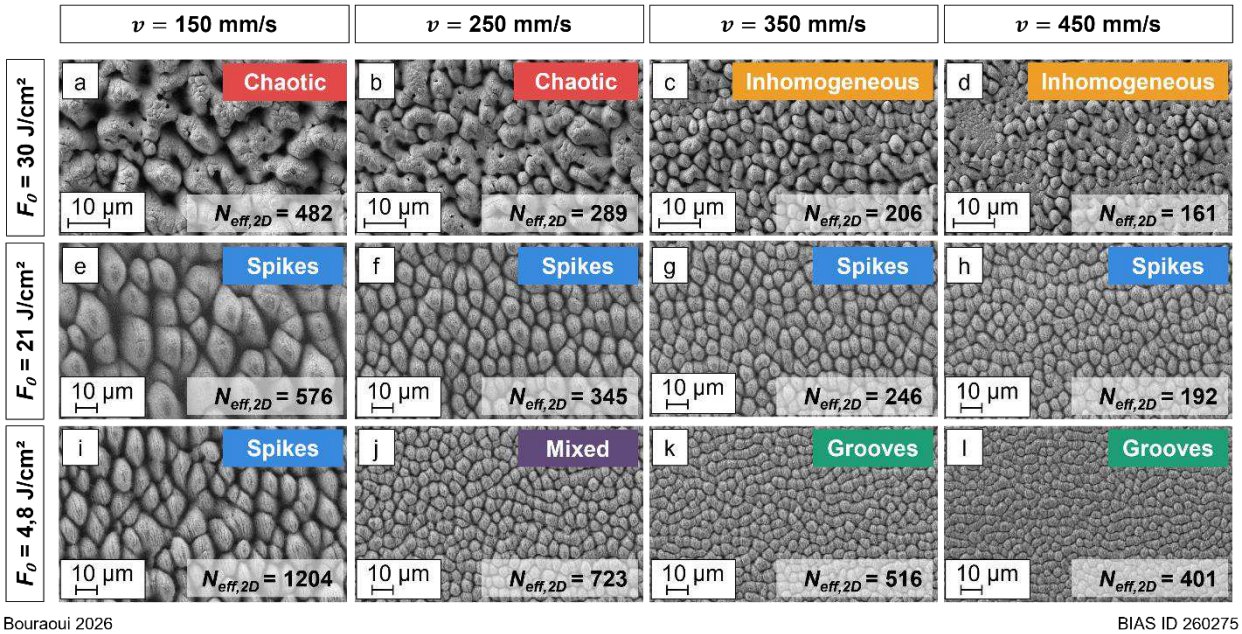

Figure 3: Representative SEM images of the surface morphologies obtained at 100 kHz for peak fluences F_0 of 4.8 J/cm², 21.1 J/cm² and 30.1 J/cm². The corresponding processing conditions are indicated in the individual images.

The complete morphology map is summarized in *Figure 4* as a function of peak fluence F_0 and effective pulse number $N_{eff,2D}$ for repetition rates of 100 kHz and 50 kHz. The three peak fluence levels were obtained using beam diameters of 115 µm, 55 µm and 46 µm for 4.8 J/cm², 21.1 J/cm² and 30.1 J/cm², respectively. The line overlap was fixed at 95% of the applied beam diameter, resulting in corresponding line distances of 5.75 µm, 2.75 µm and 2.30 µm. At a given scan velocity and repetition rate, the different beam diameters therefore also resulted in different $N_{eff,2D}$ values and different spatial extents of the Gaussian fluence distribution. The plotted effective number of pulses represents discrete investigated processing conditions resulting from the applied parameter combinations. At 4.8 J/cm² and 100 kHz, grooves are obtained at the lower investigated values up to an effective number of pulses of 602. A mixed texture having equal spikes and grooves contributions occurs at an effective number of pulses of 723 and the first pure spikes are obtained at the next investigated value of 904. At 50 kHz, grooves are obtained at the lower investigated conditions up to an effective number of pulses of 452, whereas the next investigated condition at 602 is classified as spikes. For a peak fluence of 21.1 J/cm², spikes are obtained over a broader range of the investigated effective number of pulses at both repetition rates. At 100 kHz, grooves are obtained at the lower investigated exposures up to an effective number of pulses of 173. The next investigated value of 192 produces a mixed texture, while the higher investigated exposures produce spikes. At 50 kHz, grooves are obtained up to an effective number of pulses of 144, whereas the next investigated value of 173 leads to spikes. Consequently, the matched condition with an effective number of pulses of 173 results in grooves at 100 kHz and spikes at 50 kHz.

At 30.1 J/cm², all obtained textures at 50 kHz are classified as inhomogeneous. At 100 kHz, inhomogeneous textures occur from 131 to 206 pulses, while chaotic textures form at the higher investigated value starting from 241 pulses. Thus, these chaotic textures are observed only at 100 kHz within the investigated parameter range. Chaotic textures were considered outside the defined process window and were excluded from the subsequent spatial period evaluation.

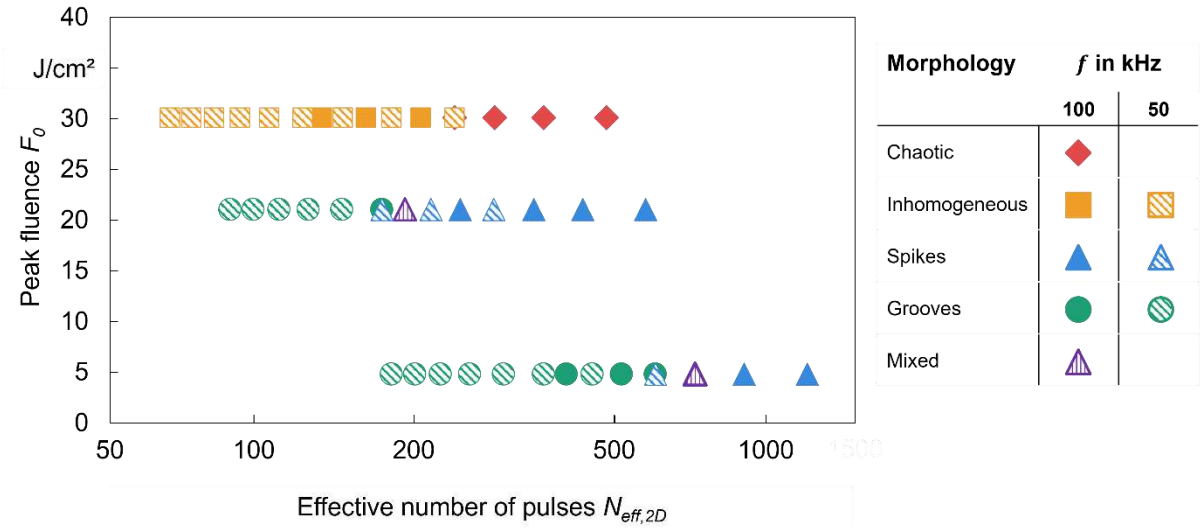

Bouraoui 2026 BIAS ID 260276

Figure 4: Morphology map of the laser structured surfaces as a function of peak fluence F_0 and effective number of pulses $N_{eff,2D}$. Symbols indicate the primary morphology classification, where Filled symbols represent stand for 100 kHz and hatching for 50 kHz. Both mixed textures were obtained with 100 kHz.

Figure *5* shows representative SEM images and the corresponding spectral distributions for pure spikes and grooves textures. The yellow dashed circle in the 2D-FFT maps represents the reference laser wave vector k_λ. The spikes textures in Figure 5.a-b exhibit spectral power concentrated close to the origin and inside the reference circle. The larger, elongated and non-uniform spikes in Figure 5.a produce a slightly anisotropic, oval-shaped spectral distribution, while the rounder and more uniform spikes in Figure *5*.b produce a more circular, quasi-isotropic spectral feature and shift to higher wave vectors. The grooves textures in Figure 5.c-d result in directional spectral features at higher wave vectors than spikes textures. In Figure 5.c, these features are broader and only slightly separated. In Figure 5.d, the spectral features are more clearly separated and appear to have a preferential direction. A second spectral contribution occurs at larger spatial wavenumbers outside the reference circle and is assigned to the LIPSS. The LIPSS spectral features are oriented orthogonally to the grooves. Moreover, LIPSS features are more pronounced in Figure 5.d compared to those in Figure *5*.c. LIPSS are also present on spikes textures. Their direct visibility in the SEM images in Figure 5.a-b is reduced by the lower magnification used to include a larger number of spikes.

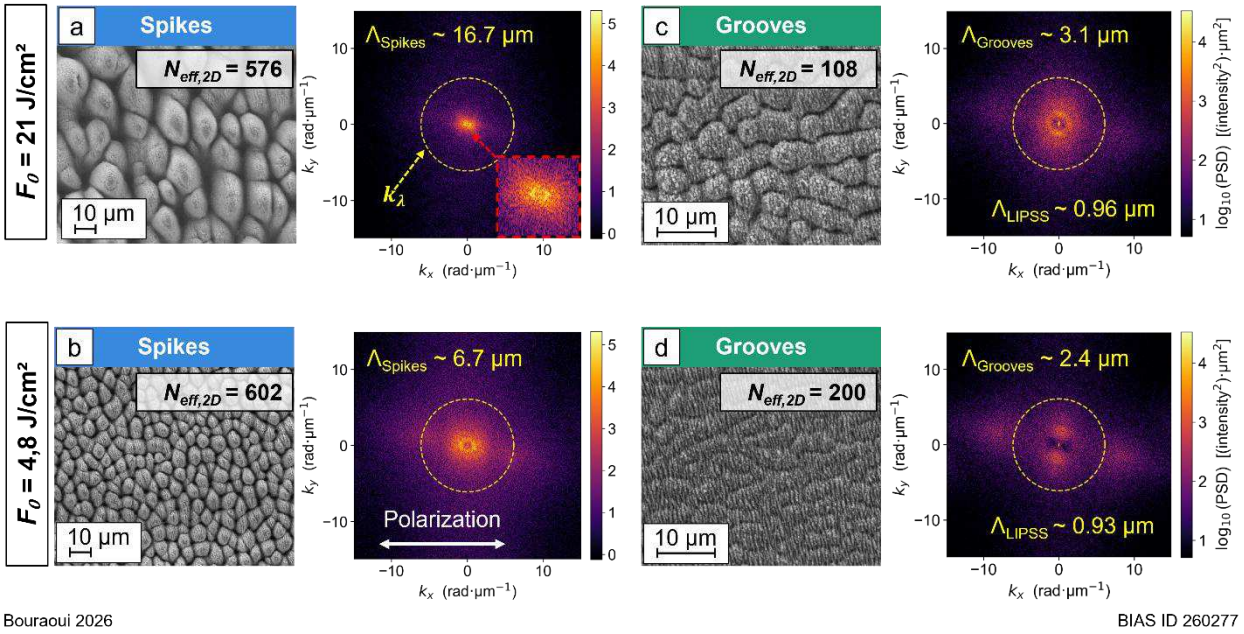

Figure 5: Representative SEM images and corresponding 2D-FFT spectral distributions of (a-b) spikes and (c-d) grooves textures. The yellow dashed circle indicates the reference laser wavenumber k_λ.

The characteristic spatial periods of spikes and grooves as a function of the effective number of pulses are depicted in Figure 6.a-b and Figure 6.c-d, respectively. The LIPSS period was evaluated separately and remains approximately constant across the investigated processing parameters and morphology classes, ranging from approximately 0.88 µm to 0.96 µm. At 4.8 J/cm², the spikes period increases with the effective number of pulses at 100 kHz, ranging from 6.31 µm ± 0.72 µm to 12.21 µm ± 1.26 µm. At 50 kHz, the spikes textures exhibit a spatial period of 6.70 µm ± 0.72 µm. At the same fluence, the grooves vary within a comparatively limited range. Values from approximately 2.4 µm to 3 µm are obtained at both repetitions rates. Thus, higher numbers of pulses showed weaker influence on grooves evolution at 4.8 J/cm². The mixed texture obtained at 4.8 J/cm² and 100 kHz exhibits a spikes period of 6.31 µm ± 0.72 µm and a grooves period of 4.04 µm ± 2.62 µm. At 21.1 J/cm², spikes periods up to 16.72 µm ± 1.85 µm and 13.20 µm ± 1.40 µm are obtained for 100 kHz and 50 kHz, respectively. Grooves are obtained at the lower investigated effective number of pulses at 21.1 J/cm². At 100 kHz a spatial period of 4.14 µm ± 2.62 µm is recorded. With an increase in the effective number of pulses at 50 kHz, the grooves period ranges from 2.67 µm ± 1.33 µm to 3.65 µm ± 2.23 µm. At 21.1 J/cm² and 100 kHz, the mixed texture results in a spikes period of 6.73 µm ± 0.73 µm and a grooves period of 4.02 µm ± 2.68 µm. For a peak fluence of 30.1 J/cm², the investigated inhomogeneous textures contain grooves and spikes with different dominance depending on the processing parameters. At 100 kHz, all evaluated inhomogeneous textures are spikes-dominated, with characteristic spikes periods ranging from 20.10 µm ± 2.32 µm to 28.55 ± 3.36 µm. At 50 kHz, the morphology changes from grooves-dominated textures through a mixed texture to spikes-dominated textures with an increase in the effective number of pulses. The characteristic grooves periods of the grooves-dominated textures range from 4.26 µm ± 2.96 µm to 7.27 µm ± 7.84 µm. For the spikes-dominated textures, the characteristic spikes periods extend from 20.11 µm ± 2.21 µm to 27.81 µm ± 2.83 µm. At 30.1 J/cm² and 50 kHz, the inhomogeneous mixed texture exhibits characteristic periods of 18.40 µm ± 2.15 µm for the spikes and 6.72 µm ± 6.83 µm for the grooves.

It should be noted that the FFT analysis of inhomogeneous textures may yield larger apparent grooves and spikes periods because the determined periodicity can include the spatial separation between clusters of the same morphology in addition to the characteristic period within individual clusters.

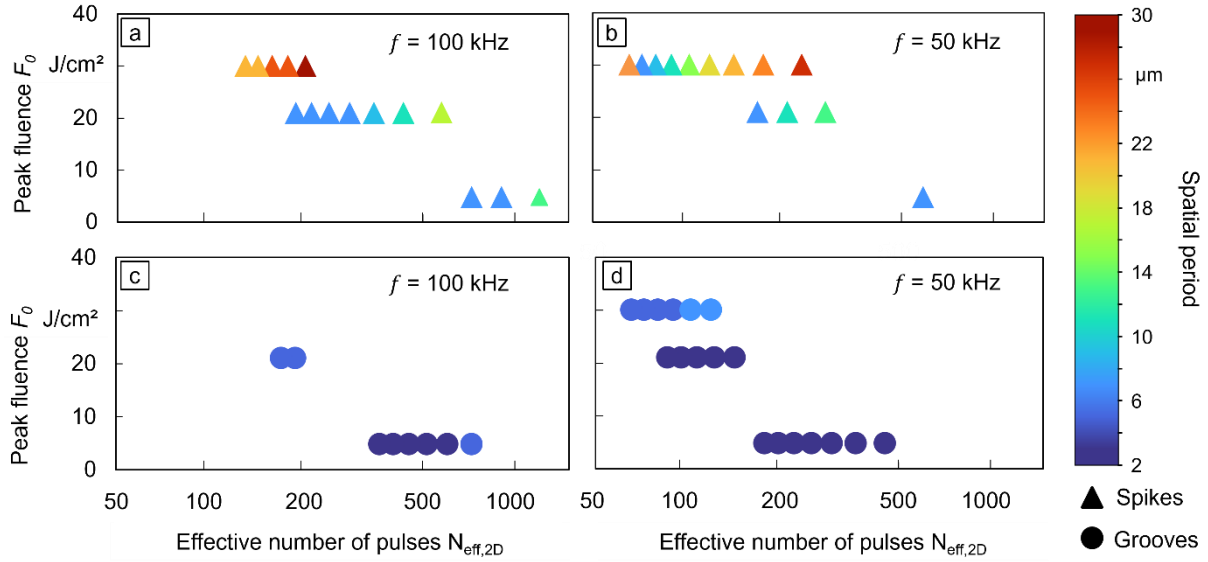

Bouraoui 2026

BIAS ID 260278

Figure 6: Characteristic spatial periods of (a-b) spikes and grooves (c-d) as a function of peak fluence F_0 and effective number of pulses $N_{eff,2D}$. Color bar indicates the spatial period in µm.

To evaluate the influence of repetition rate under comparable accumulated exposure, nine matched processing pairs were compared. For each pair, F_0 and $N_{eff,2D}$ were identical and the pulse-to-pulse displacement v/f was maintained, while the inter-pulse interval changed from 10 µs at 100 kHz to 20 µs at 50 kHz. The resulting morphologies, characteristic periods and relative differences are summarized in Table 2 and Figure 7 shows SEM images of selected matched pairs.

Table 2: Process parameters of nine matched conditions used to evaluate the influence of repetition rate and their corresponding generated morphology and relative difference.

F_0	$N_{eff,2D}$	v (100/50 kHz)	Pulse-to-pulse displacement v/f	Morphology Λ (100 kHz)	Morphology Λ (50 kHz)	Relative difference
J/cm²	-	mm/s	µm	- / µm	- / µm	%
4.8	361	500/250	5	Grooves 2.82 ± 1.40	Grooves 2.79 ± 1.42	0.9
4.8	452	400/200	4	Grooves 2.80 ± 1.45	Grooves 3.00 ± 1.73	7.0
4.8	602	300/150	3	Grooves 2.98 ± 1.61	Spikes 6.70 ± 0.72 µm	76.9
21.1	173	500/250	5	Grooves 4.14 ± 2.62	Spikes 7.75 ± 0.77	60.8
21.1	216	400/200	4	Spikes 7.06 ± 0.76	Spikes 10.51 ± 1.08	39.2
21.1	288	300/150	3	Spikes 7.56 ± 0.85	Spikes 13.20 ± 1.40	54.3
30.1	145	500/250	5	Inhomogeneous, spikes-dominated 21.49 ± 2.38	Inhomogeneous, spikes-dominated 20.11 ± 2.21	6.7
30.1	181	400/200	4	Inhomogeneous, spikes-dominated 25.08 ± 2.74	Inhomogeneous, spikes-dominated 22.44 ± 2.47	11.1
30.1	241	300/150	3	Chaotic texture	Inhomogeneous, spikes-dominated 27.81 ± 2.83	—

At 4.8 J/cm², the matched grooves with effective numbers of pulses of 361 (see Figure 7.g-h) and 452 exhibit similar spatial periods at both repetition rates with relative differences of 0.9% and 7.0%, respectively. At the higher matched value of 602, the morphology differs, with grooves obtained at 100 kHz and spikes at 50 kHz. For a peak fluence of 21.1 J/cm², the morphology differs at the lowest matched effective number of pulses of 173 with grooves obtained at 100 kHz and spikes at 50 kHz, see Figure 7.e-f. At the higher matched values of 216 and 288 (see Figure 7.c-d), spikes are obtained at both repetition rates, with larger characteristic periods at 50 kHz than at 100 kHz and relative differences of 39.2% and 54.3%, respectively. At 30.1 J/cm², the matched inhomogeneous, spikes-dominated textures with effective numbers of pulses of 145 and 181 exhibit relative period differences of 6.7% and 11.1%, respectively. With an increase to the higher matched value of 241, the 100 kHz surface exhibits a chaotic texture, whereas the 50 kHz surface remains inhomogeneous and spikes-dominated, see Figure 7.a-b. At 30 J/cm^2 and 4.8 J/cm^2 the scan velocity pairs of 150/300 mm/s led to strong deviations, while at 21.1 J/cm^2 all matched conditions were different in morphology classes or characteristic periods.

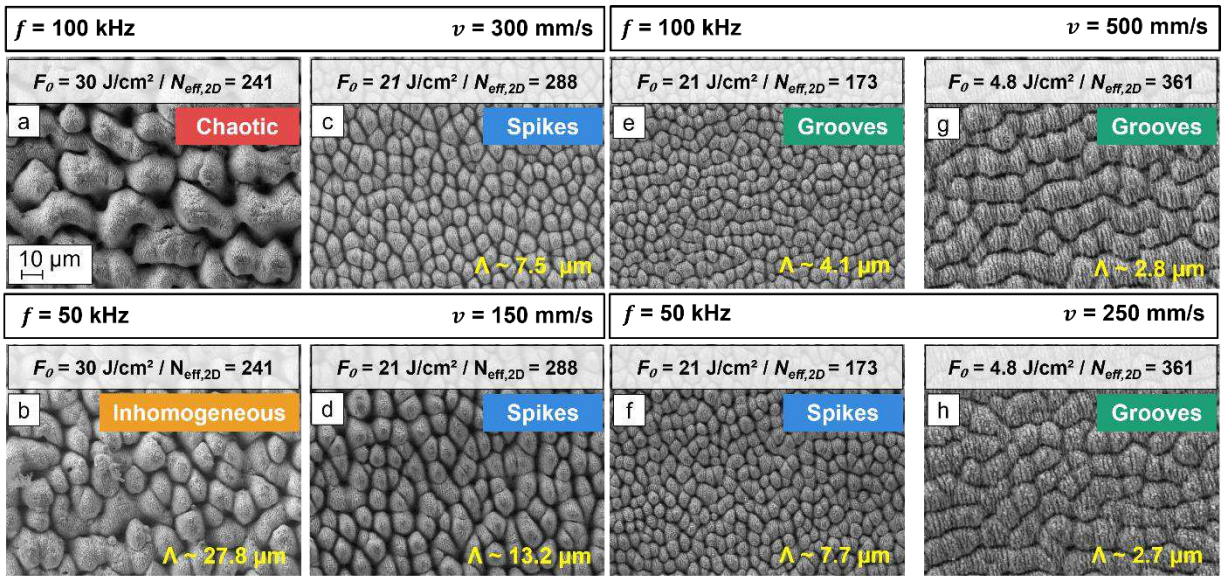

Figure 7: Representative SEM images of selected matched F_0 / $N_{eff,2D}$ processed at 100 kHz and 50 kHz, illustrating repetition rate related differences in morphology and characteristic spatial period.

Figure 8 compares cross sections of surfaces generated with different parameters combinations. Figure 8.a shows a chaotic texture and Figure 8.b shows an inhomogeneous, spikes-dominated texture, while Figure 8.c and Figure 8.d compares matched conditions at 100 kHz and 50 kHz, respectively. Despite the different morphology classes and processing conditions, the cross sections show the same characteristic position relative to the initial surface. The protruding structures and the depressions between them are located below the initial surface level in all investigated samples.

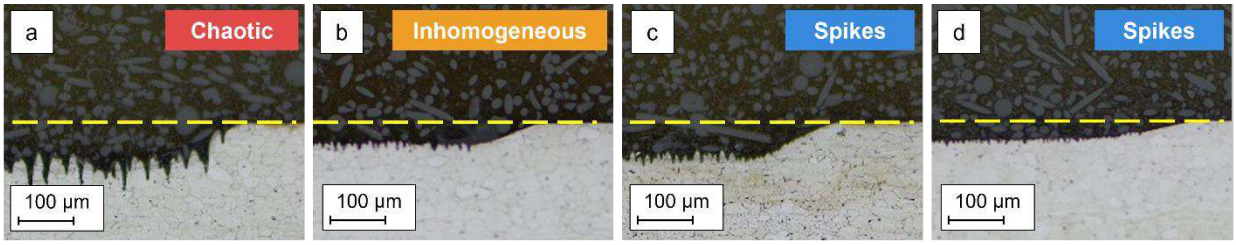

Figure 8: Cross-sectional overview of selected textures processed under different peak fluence, number of pulses and repetition rate combination: (a) chaotic texture (30.1 J/cm² / 482 / 100 kHz), (b) inhomogeneous spike-dominated texture (30.1 J/cm² / 240 / 50 kHz), (c) spikes (21.1 J/cm² / 288 / 100 kHz) and (d) spikes (21.1 J/cm² / 288 / 50 kHz). The yellow dashed line indicate the neighboring untreated surface level.

Figure 9 shows tilted cross-sectional SEM images of different morphologies and their corresponding microstructural images. Despite the differences in surface topography, no visible alteration of the microstructure is observed between the structured regions and the underlying bulk material.

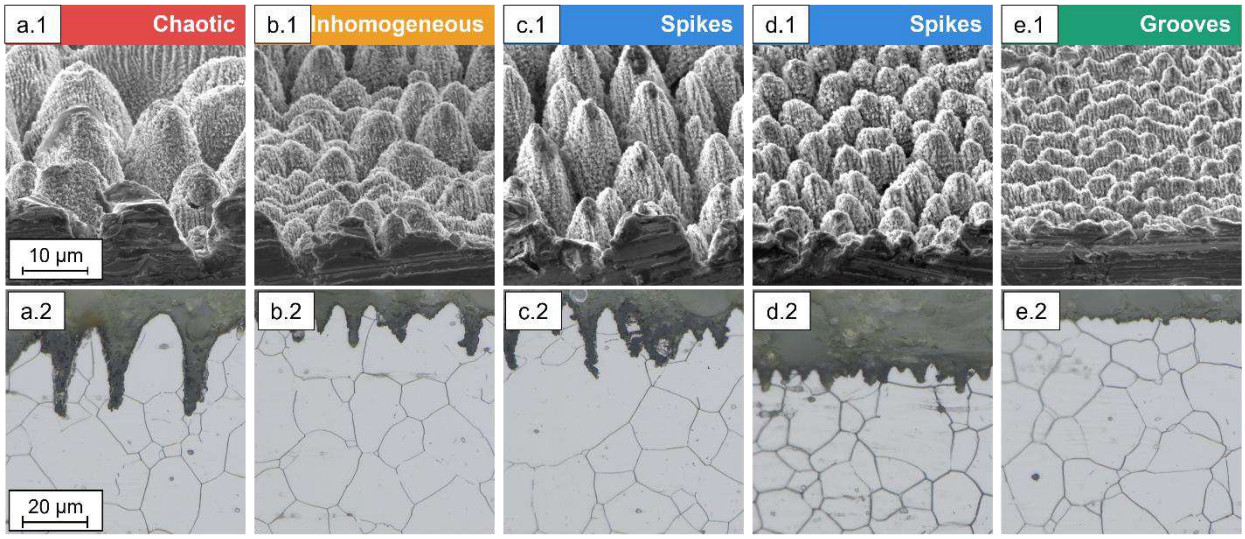

Bouraoui 2026 BIAS ID 260282

Figure 9: Tilted cross-sections of (a.1) chaotic texture (30.1 J/cm² / 289 / 100 kHz), (b.1) inhomogeneous spike-dominated texture (30.1 J/cm² / 145 / 50 kHz), (c.1) spikes (4.8 J/cm² / 1204 / 100 kHz), (d.1) spikes (4.8 J/cm² / 602 / 50 kHz) and (e.1) grooves (4.8 J/cm² / 401 / 100 kHz) and (a.2-e.2) their corresponding microstructural analysis.

In Figure 10. and Figure 10.b, the structuring rate ranges associated with the different morphology regimes are depicted for 100 kHz and 50 kHz, respectively. Since the decrease in peak fluence levels was performed through beam diameter enlargement at a fixed 95%-line overlap. The larger beam diameter used at 4.8 J/cm² therefore resulted in the highest investigated structuring rates. At 4.8 J/cm², the transition from grooves toward spikes occurs at 0.518 cm²/min and 1.035 cm²/min at 50 kHz and 100 kHz, respectively. The highest structuring rate obtained for grooves was 1.725 cm²/min at both repetition rates. At 21.1 J/cm², the transition toward grooves occurred at 0.413 cm²/min and 0.825 cm²/min, depending on the repetition rate. At 100 kHz, spikes extended to higher structuring rates than at 50 kHz. At 30.1 J/cm², the evaluated conditions remained within the inhomogeneous regime. At 50 kHz, the dominant morphology changed from spikes at lower structuring rates through mixed grooves and spikes at 0.414 cm²/min to grooves from 0.483 cm²/min to 0.759 cm²/min. At 100 kHz, the evaluated inhomogeneous textures remained spikes-dominated over the corresponding structuring-rate range.

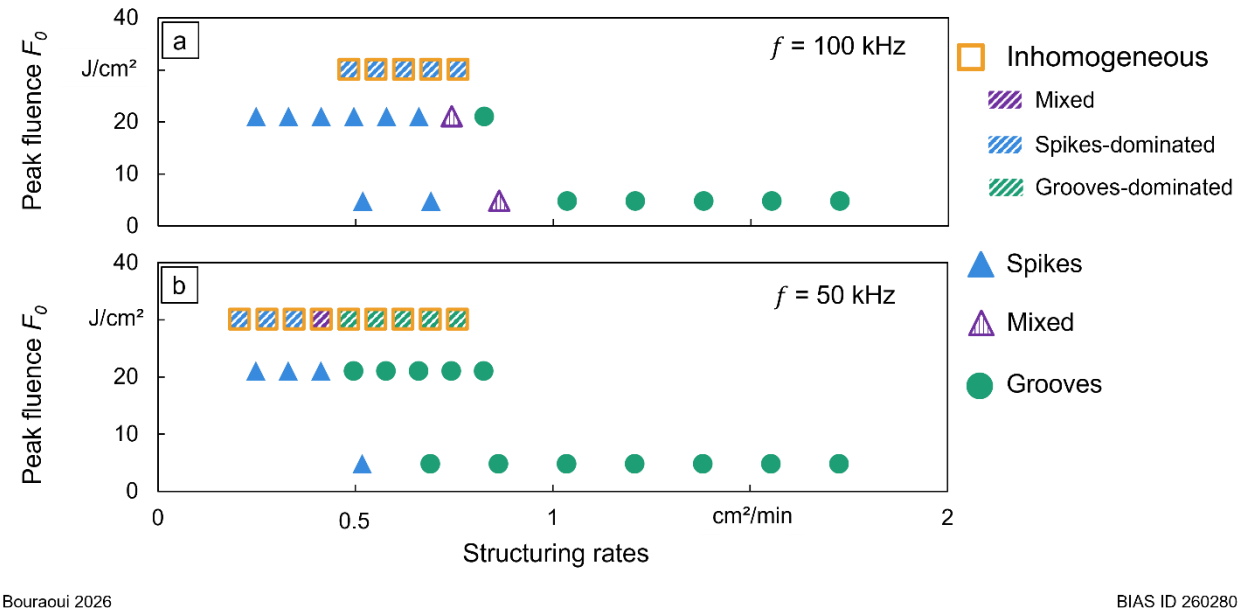

Figure 10: Areal structuring rate as a function of peak fluence F_0 for (a) 100 kHz and (b) 50 kHz. Filled symbols indicate homogeneous spikes, mixed textures and grooves. Orange square outlines identify inhomogeneous textures, while the hatching indicates the domiance.

4. Discussion

4.1 Influence of processing parameters on morphology formation

The morphology map in Figure 4 shows that the resulting surface morphology changes systematically with the combined variation of peak fluence F_0 and effective pulse number $N_{eff,2D}$. At 4.8 J/cm², the investigated conditions progress from grooves at lower pulses, through a mixed groove–spikes texture at 723, to spikes at the higher investigated exposures with the first pure spikes texture occurring at the next investigated value of 904. At F_0 = 21.1 J/cm², the same general progression occurs at substantially lower $N_{eff,2D}$ and spikes consequently occupy a broader range of the investigated conditions. Thus, increasing F_0 shifts the transition from grooves toward spikes to lower accumulated pulse exposure. The different peak fluence levels were generated by changing the beam diameter through defocusing. Increasing the beam diameter at constant pulse energy reduces the peak fluence and broadens the Gaussian fluence distribution, resulting in a less pronounced fluence gradient across the irradiated area. In contrast, the smallest beam diameter results in the highest central peak and a stronger spatial variation in fluence. Since the line overlap was fixed at 95% of the applied beam diameter, enlarging the beam diameter also increases the line distance. At fixed scan velocity and repetition rate, it also changes and the $N_{eff,2D}$. The influence of the beam profile was reported for femtosecond surface texturing of stainless steel, where increasing the spot diameter promoted a more homogeneous energy distribution [23]. These effects may contribute to the broader formation window of homogeneous textures at the larger beam diameters, while the stronger fluence variation at the smallest beam diameter may contribute to the inhomogeneous and chaotic textures observed at 30.1 J/cm².

Several studies investigated the influence of the fluence and accumulated pulse exposure on the resulting morphology for laser-structured metals. Kirner et al. reported grooves as an intermediate morphology between LIPSS and spikes when varying fluence and effective pulse number [24],

while Baron et al. observed a progression from spikes toward irregular structures with further increasing the repeated irradiation [25]. These studies demonstrate the dependence of morphology evolution on the peak fluence and effective number of pulses observed in Figure 4 as combined irradiation effects. Importantly, the exposure quantities used in these studies are not necessarily equivalent. The mixed grooves-spikes textures in Figure 4 further indicate that the transition between these morphology regimes occurs progressively as the irradiation conditions are varied. Similar intermediate morphologies containing characteristics of both grooves and spikes have been experimentally observed within transition regions of morphology maps [24]. Furthermore, the significantly different $N_{eff,2D}$ at which this transition occurred at 4.8 J/cm² and 21.1 J/cm² further demonstrates that a higher peak fluence requires less accumulated exposure within the investigated parameter space to reach the transition toward spikes.

The LIPSS superimposed on the larger grooves and spikes in Figure *3* are consistent with the spatial fluence distribution experienced during scanning with a Gaussian beam. Individual surface positions are irradiated by the lower fluence peripheral regions of the Gaussian beam [26]. Previous work describes hierarchical surfaces containing LIPSS on larger grooves and spikes in terms of these different local fluence ranges [27].

At the highest investigated peak fluence of 30.1 J/cm², Figure 4 shows a departure from the homogeneous grooves and spikes regimes. All investigated conditions produce inhomogeneous textures, with the dominant morphology varying between grooves, mixed grooves-spikes and spikes depending on the effective number of pulses and repetition rate. At 100 kHz, the higher investigated $N_{eff,2D}$ additionally result in chaotic textures. Consequently, increasing accumulated exposure at this fluence leads to increasingly disrupted surface organization.

Ahmmed et al. observed a comparable evolution on AISI 304 and showed that rough and rugged chaotic structures occur at high combinations of fluence and accumulated irradiation. In their experiments, grooves and spikes-like microstructures occupied lower irradiation ranges, but a significant increase in the accumulated fluence produced chaotic structures. The authors related the occurrence of chaotic textures to the combined spatial accumulation of successive pulses and neighboring scan lines rather than to pulse fluence alone [28].

Ling et al. investigated this regime in more detail on AISI 304 and separated the observed morphologies into a low-fluence and a high-fluence regime. The high-fluence regime contained columnar and chaotic structures, with the chaotic textures characterized by the absence of a periodic pattern. In contrast to the continuously evolving ellipsoidal cones at lower fluence, the columnar and chaotic structures did not significantly change with additional laser scans, indicating that the surface morphology was largely established during the initial irradiation. Ling et al. associated this high-fluence regime with more complex ablation conditions involving processes such as plasma-plume formation and expansion but explicitly did not assign a single formation mechanism to the chaotic structures [6]. The spatial distribution of accumulated irradiations may additionally contribute to the reduced homogeneity observed at 30.1 J/cm² in the morphology map in Figure 4. Schnell et al. experimentally demonstrated that pulse overlaps in the scanning direction and line overlap in the transverse direction influence the homogeneity of laser generated surface structures [12]. Their results support the general sensitivity of texture homogeneity to the spatial distribution of accumulated pulses and therefore could present a possible cause for the inhomogeneity observed in this study. The effective pulse number describes the accumulated spatial exposure but does not uniquely specify how this exposure is delivered. Nyenhuis et al.

showed that different spatial and temporal pulse-delivery conditions can produce different surface morphologies even at comparable accumulated irradiation and related these differences to the spatiotemporal irradiation history and heat accumulation [16].

4.2 Spectral characteristics and evolution of the spatial period

The spikes morphologies in Figure 3 and Figure 5.a-b evolve from larger, elongated structures with pronounced variations in size and shape toward more uniformly rounded and smaller spikes with decreasing $N_{eff,2D}$. This morphological change is reflected in the corresponding 2D-FFT maps. The elongated and less uniform spikes in Figure 5.a produce a slightly anisotropic, oval-shaped spectral distribution close to the origin, while the more uniformly rounded spikes in Figure 5.b produce a circular, quasi-isotropic spectral feature at higher wavenumbers. Comparable results were published by Kam et al., where the authors distinguished between the conditions determining whether spikes initially form and those controlling their subsequent dimensions and distribution. They suggested that initial spikes formation is primarily governed by the fluence applied, whereas their final dimensions additionally depend on their response to repeated scanning. They observed different formations under near-threshold and high-fluence processing. At near-threshold fluence levels, spikes appear progressively and randomly across the surface, while at high-fluence levels they develop simultaneously. Once spikes are formed, their number density and resulting dimensions changed with subsequent accumulated exposure, where larger structures appeared at lower scan velocities. In their high-fluence regime, they related this behavior to the overlapping Gaussian fluence profiles during scanning. Varying the scan velocity changes the spatial pulse overlap and consequently the irradiation delivered to each position [19]. In the current study, the evolution toward smaller spikes dimensions and different spatial organization with increased scan velocities (lower $N_{eff,2D}$) in Figure *3* and Figure *5* is consistent with this experimental observation that the final spikes texture continues to develop after the spikes' regime has been reached. The spatial periods of the resulting morphologies will be discussed in detail later.

The elongated spikes at higher $N_{eff,2D}$ observed in Figure *3*.e,i and Figure *5*.a additionally exhibit a preferred orientation, with their longer axis perpendicular to the linear laser polarization. This polarization dependence differs from the strong polarization dependence of LIPSS and grooves that is already well established. In fact, spikes show a weak correlation with laser polarization [24]. Although, Zhu et al. demonstrated that linearly polarized femtosecond irradiation can generate elliptically shaped spikes with their long axes perpendicular to the polarization, while circular polarization produced symmetric spikes [29]. The orientation observed in our study indicates that polarization can influence the later geometrical evolution of spikes, although this dependence is less consistently reported than for LIPSS and grooves.

The grooves textures in Figure *5*.c-d are characterized by elongated directional spectral features located inside the reference laser wavenumber circle. Nyenhuis et al. identified the corresponding grooves spectral characteristics as the type-g signal and distinguished it from the type-s signal associated with LIPSS. With decreasing scan velocity, they observed that grooves progressively merged, resulting in stronger type-g features that shifted toward the center of the FFT map. The shift toward smaller wavevectors corresponds to an increase in the characteristic grooves period. At the same time, the dominance of the type-g signal became more pronounced, while the LIPSS-related type-s signal decreased as grooves developed on the surface [16].

The evolution in Figure *5*.c-d shows similar behavior. With increasing scan velocity, the grooves spectral features are located further from the origin, indicating a smaller characteristic grooves period, while the strength of LIPSS signal became more comparable to grooves signal. This indicates that Figure *5*.d represents a transitioning state from grooves toward LIPSS. This agrees with the evolution reported by Nyenhuis et al. [16].

Furthermore, the orientation relative to the laser polarization distinguishes the two hierarchical structures in Figure *5*.c-d. The grooves and LIPSS are aligned parallel and orthogonal to the laser polarization, respectively. Additionally, the LIPSS periods ranging from 0.88 µm to 0.96 µm correspond to approximately $0.85 * \lambda$ and $0.93 * \lambda$ for the applied wavelength of 1030 nm. Periods slightly below the irradiation wavelength combined with an orientation perpendicular to the laser polarization are characteristic of LSFL-LIPSS on metals. Periods slightly below the irradiation wavelength combined with an orientation perpendicular to the laser polarization are characteristic of LSFL on metals [26]. The superposition of LSFL and larger grooves is also consistent with the hierarchical development from LSFL to grooves reported by Nyenhuis et al. [16]. The LIPSS periods also remain within this narrow range across the different processing conditions, independent of the underlying dominant morphology. Studies on steel have similarly reported stable LIPSS periods despite changes in accumulated irradiation or repetition rate [30]. In contrast to the pronounced evolution of the spikes and grooves discussed below, LIPSS are comparatively insensitive to the processing variations investigated here.

The period analysis in Figure 6 further shows that the continued morphological development of spikes is accompanied by a change in their characteristic spatial period. Across the investigated spikes conditions at 4.8 J/cm² and 100 kHz and at 21.1 J/cm² at both repetition rates, higher number of pulses led to larger spikes periods. This continued development after initial spike formation is consistent with the changes in spike dimensions with accumulated pulse exposure reported by Kam et al. [19]. Fraggelakis et al. reported growth and densification of conical structures with increasing pulse exposure [9]. Gomez-Munoz et al. also observed increasing characteristic dimensions of spike-like structures with increasing effective pulse number [31].

The mixed textures contain two simultaneously measurable supra-wavelength periods. At both 4.8 J/cm² and 21.1 J/cm², the spikes periods in the mixed conditions remain substantially smaller than those reached by spikes at the higher investigated number of pulses, while the grooves and spikes periods are comparatively close to one another. This further indicates their location within the grooves to spikes transition identified in Figure 4. Mixed grooves-spikes morphologies have similarly been observed in transition regions between the two structure regimes [24]. In the present work, the simultaneous occurrence of both characteristic periods and their relative proximity provide a quantitative analysis for the progressive grooves to spikes transition in which the emerging spikes have not yet developed toward the larger characteristic dimensions reached within the established spikes regime. The grooves periods at 4.8 J/cm² remain within a comparatively narrow range between approximately 2.4 and 3.0 µm across the investigated conditions. At 21.1 J/cm² and 100 kHz, the grooves periods increase up to approximately 4 µm. Therefore, grooves do not exhibit the same pronounced and systematic evolution as spikes under the investigated conditions. Nevertheless, grooves are sensitive to irradiation. A systematic grooves development with increasing numbers of scans and pulses was reported in other investigations [16,32].

At 30.1 J/cm², the inhomogeneous textures exhibit significantly different periods depending on the processing condition. The periods of grooves-dominated textures are larger than those of the homogeneous grooves obtained at lower fluence levels. As mentioned earlier, the FFT analysis of inhomogeneous textures may result in larger apparent grooves and spikes periods the spatial separation between clusters of the same morphology in addition to the characteristic period within individual clusters.

The matched pairs in Figure 7 and Table 2 show that repetition rate affects the texture dimensions differently depending on the morphology regime. At 4.8 J/cm², the matched grooves have relative period differences below 10%, whereas at the higher matched $N_{eff,2D}$ the morphology differs between grooves at 100 kHz and spikes at 50 kHz. At 21.1 J/cm², the effect extends to the periods of developed spikes. At the two matched conditions, where both repetition rates produce spikes, their periods are approximately 39% and 54% larger at 50 kHz. Thus, repetition rate affects both the position of the grooves to spikes transition and the characteristic lateral scale within the spikes regime. At 30.1 J/cm², the surface shows a different response. The matched spikes-dominated inhomogeneous textures at $N_{eff,2D}$ of 145 and 181 have comparatively similar characteristic periods. However, at 241, a chaotic texture and an inhomogeneous spikes-dominated texture are obtained at 100 kHz and at 50 kHz, respectively. Consequently, the influence of the repetition rate changes across the process range. Within the homogeneous structures' regimes, it is reflected in the characteristic periods, while close to morphologies boundaries, it impacts the stability of the morphology itself. For these matched pairs, the pulse-to-pulse spatial displacement v/f is identical, but the temporal interval between successive pulses changes from 10 µs at 100 kHz to 20 µs at 50 kHz. Consequently, the surface region irradiated by a subsequent pulse experiences different thermal history. Bauer et al. reported altered heat accumulation effects during scanning ablation of stainless steel using 6 ps pulses at 1030 nm. Their model demonstrated that both the temporal pulse separation and the spatial displacement influence the thermal state at the location of subsequent irradiation and subsequently the resulting material response [11]. Nyenhuis et al. similarly demonstrated that changing the temporal and spatial delivery of pulses can significantly modify texture development and related this to differences in heat accumulation [16]. The larger spikes periods at 50 kHz and 21.1 J/cm² can be related to the longer pulse interval and the resulting difference in the thermal state. The 20 µs interval at 50 kHz allows thermal energy to diffuse over a larger characteristic distance before the following pulse arrives, compared to the 10 µs interval at 100 kHz. These results show that equal accumulated exposure does not necessarily lead to the same texture, when the spatial and temporal pulse delivery differs.

4.3 Formation and development of spikes

The cross-sectional analysis in Figure 8 reveals that the complete structured profiles remain below the initial surface level, including both the protruding structures and the surrounding depressions. This behavior is observed for all investigated morphologies and processing conditions. The microstructural analysis in Figure 9 further shows no visible difference between the structured regions and the underlying bulk material. Zuhlke et al. addressed the formation mechanism of spikes during stepped-growth experiments on nickel. They distinguished below-surface growth (BSG), in which the structure peaks remain below the original surface, from above-surface growth (ASG), in which the structures extend above it. The authors suggested that the structures result from several mechanisms rather than from one single process. Preferential valley ablation associated with scattering and geometrical effects, surface-melt flow and redeposition were all

observed, but their relative dominance depended on fluence and pulse exposure. Preferential valley ablation was the dominant mechanism for BSG. ASG mainly resulted from material flow and redeposition. They reported BSG structures as a common dominant mechanism of self-organized spikes on metals under femtosecond processing. Therefore, the below-surface position observed in Figure 8 provides geometrical evidence consistent with a BSG-type mechanism under the present conditions. Zuhlke et al. separated BSG development into three phases. In phase 1, the surface roughness was increased which modified the energy distribution of subsequent pulses, leading to micro-ripples oriented parallel to the laser polarization providing precursor sites for spikes along their peaks. Their dimensions and orientation are morphologically comparable to the grooves observed here. In phase 2, preferential valley ablation becomes dominant. The inclined sidewalls receive a lower local fluence than the valleys, causing differential ablation and increasing the relative height and width of the structures, while the entire structure recedes. In phase 3, formed structures continue to grow laterally and merge with increasing pulse numbers. This could explain the increasing spikes period with accumulated exposure in Figure 6 and the progression from smaller spikes toward larger spikes [18]. Moreover, the microstructure analysis in Figure 9 is consistent with the results reported by Ling et al. on femtosecond generated ellipsoidal cones on AISI 304. In their experiments, the microstructure grains extended continuously from the substrate into the cones without an interface separating the structures from the underlying material. They concluded that the cones consisted principally of unablated steel. Their analysis also showed that the conical geometry reduced the local fluence on the inclined surfaces, resulting in preferential ablated surrounding area [33]. Another possible contribution is the laser-material interaction with subsequent irradiation during continuous developing topography. Nyenhuis et al. proposed that spikes inclination reduces the projected incident fluence on the slopes, while reflections within the structured surface can locally increase the fluence inside the depressions. Preferential removal inside the grooves could then contribute to the excavation of larger protruding structures [16].

On the other hand, polarization may also contribute to the directional development of the different hierarchical morphologies. In the present study, grooves are oriented parallel to the linear polarization and the LSFL perpendicular to it, while the elongated spikes at higher accumulated exposure have their long axis perpendicular to the polarization. For the larger spike morphology, Zhu et al. reported that linearly polarized irradiation produced elliptical conical spikes whose long axes were perpendicular to the polarization and circular polarization produced approximately symmetric conical spikes. They attributed this anisotropy to the different Fresnel transmission of the local p- and s-polarized components on the inclined spike surfaces. The resulting azimuthal variation in transmitted energy leads to different ablation rates around the spikes and therefore to elongation perpendicular to the polarization [29].

4.4 Structuring rates

Figure 9 shows that increasing the structuring rate is associated with changes in the resulting morphology. At 4.8 J/cm² and 21.1 J/cm², increasing the scan velocity and subsequently the structuring rates produce grooves. Inversely, lower structuring rates lead to the transition toward spikes. The higher maximum structuring rates obtained at 4.8 J/cm² result directly from the larger beam diameter and therefore larger line distance used at the fixed 95% overlap. Furthermore, the repetition rate also shifts the morphologies' boundaries. At both fluences, spikes are obtained at higher structuring rates with 100 kHz, in comparison with 50 kHz. Thus, increasing productivity does not automatically preserve morphology. However, increasing the repetition rate can improve

the processing speed for spikes textures. This improved productivity is associated with modified spikes size and shape, as discussed in Section 4.2 and shown in Figure 6.

Conclusion

In this work, a morphology map of self-organized structures generated by picosecond laser structuring of stainless steel was established. The formation of grooves and spikes is governed by the combined influence of peak fluence, accumulated spatial exposure and temporal pulse delivery. At fixed peak fluence, 50 kHz shifted spikes formation toward lower accumulated exposure compared to 100 kHz, while increasing peak fluence shifted the grooves to spikes transition toward lower accumulated exposure within the investigated parameter range. At the highest fluence, reducing the accumulated exposure resulted in spatially separated grooves and spikes clusters rather than homogeneous textures, indicating that homogeneous morphology formation requires a suitable balance between peak fluence and accumulated exposure.

The spatial characteristics of spikes were also affected by spatial and temporal energy delivery, while grooves showed a lower sensitivity. With decreasing accumulated exposure, spikes evolved from larger elongated structures with a preferred orientation relative to the polarization toward smaller, more uniform round structures. Under matched accumulated exposure but different repetition rates, spikes were larger at 50 kHz than at 100 kHz. The complementary spectral classification proposed in this work provides a systematic differentiation of transition textures containing grooves and spikes and consequently allows their assignment to one main morphology or classification as mixed texture based on their contribution. This significantly reduced classification ambiguity.

Cross-sectional observations of spikes resulting from different processing conditions consistently show the structures below the original surface and indicate a possible dominant BSG-type formation mechanism. In addition, modified energy coupling influenced by laser polarization may contribute to their directional evolution. Finally, the achievable structuring rate was associated with morphology changes, while increasing repetition rate enabled spikes at higher structuring rates but also modified their spatial characteristics.

Declarations

Ethical Approval

Not applicable.

Funding

This work was funded by the Deutsche Forschungsgemeinschaft DFG – Project Number 519202422 –“Oleophile Antihaftbeschichtungen durch Oberflächenstrukturen für Kochgeschirr“ within the DFG Transfer Project funding scheme. The authors gratefully acknowledge the financial support by the Deutsche Forschungsgemeinschaft.

Availability of data and materials

Data are published in [22]. Further data can be accessed upon request.

References

[1] J. Reif, Surface Functionalization by Laser-Induced Structuring, in: P.M. Ossi (Ed.), Adv. Appl. Lasers Mater. Sci., Springer International Publishing, Cham, 2018: pp. 63–88. https://doi.org/10.1007/978-3-319-96845-2_3.

[2] J. Bonse, S. Hohm, S.V. Kirner, A. Rosenfeld, J. Kruger, Laser-Induced Periodic Surface Structures— A Scientific Evergreen, IEEE J. Sel. Top. Quantum Electron. 23 (2017) 7581030. https://doi.org/10.1109/JSTQE.2016.2614183.

[3] K. Schwibbert, A.M. Richter, J. Krüger, J. Bonse, Laser-Textured Surfaces: A Way to Control Biofilm Formation?, Laser Photonics Rev. 18 (2024) 2300753. https://doi.org/10.1002/lpor.202300753.

[4] P.G. Grützmacher, F.J. Profito, A. Rosenkranz, Multi-Scale Surface Texturing in Tribology—Current Knowledge and Future Perspectives, Lubricants 7 (2019) 95. https://doi.org/10.3390/lubricants7110095.

[5] A.A. Ionin, S.I. Kudryashov, S.V. Makarov, L.V. Seleznev, D.V. Sinitsyn, E.V. Golosov, O.A. Golosova, Y.R. Kolobov, A.E. Ligachev, Femtosecond laser color marking of metal and semiconductor surfaces, Appl. Phys. A 107 (2012) 301–305. https://doi.org/10.1007/s00339-012-6849-y.

[6] Y. Liu, Y. Brelet, Z. He, L. Yu, B. Forestier, Y. Deng, H. Jiang, A. Houard, Laser-induced periodic annular surface structures on fused silica surface, Appl. Phys. Lett. 102 (2013) 251103. https://doi.org/10.1063/1.4812354.

[7] E. Rebollar, M. Castillejo, T.A. Ezquerra, Laser induced periodic surface structures on polymer films: From fundamentals to applications, Eur. Polym. J. 73 (2015) 162–174. https://doi.org/10.1016/j.eurpolymj.2015.10.012.

[8] E. Stratakis, J. Bonse, J. Heitz, J. Siegel, G.D. Tsibidis, E. Skoulas, A. Papadopoulos, A. Mimidis, A.-C. Joel, P. Comanns, J. Krüger, C. Florian, Y. Fuentes-Edfuf, J. Solis, W. Baumgartner, Laser engineering of biomimetic surfaces, Mater. Sci. Eng. R Rep. 141 (2020) 100562. https://doi.org/10.1016/j.mser.2020.100562.

[9] F. Fraggelakis, G. Mincuzzi, I. Manek-Hönninger, J. Lopez, R. Kling, Generation of micro- and nano-morphologies on a stainless steel surface irradiated with 257 nm femtosecond laser pulses, RSC Adv. 8 (2018) 16082–16087. https://doi.org/10.1039/C8RA01774C.

[10] B.K. Nayak, M.C. Gupta, Self-organized micro/nano structures in metal surfaces by ultrafast laser irradiation, Opt. Lasers Eng. 48 (2010) 940–949. https://doi.org/10.1016/j.optlaseng.2010.04.010.

[11] F. Bauer, A. Michalowski, T. Kiedrowski, S. Nolte, Heat accumulation in ultra-short pulsed scanning laser ablation of metals, Opt. Express 23 (2015) 1035. https://doi.org/10.1364/OE.23.001035.

[12] G. Schnell, U. Duenow, H. Seitz, Effect of Laser Pulse Overlap and Scanning Line Overlap on Femtosecond Laser-Structured Ti6Al4V Surfaces, Materials 13 (2020) 969. https://doi.org/10.3390/ma13040969.

[13] M. Mezera, Picosecond Laser-induced Periodic Surface Structures, University of Twente, 2020.

[14] F. Di Niso, C. Gaudiuso, T. Sibillano, F.P. Mezzapesa, A. Ancona, P.M. Lugarà, Role of heat accumulation on the incubation effect in multi-shot laser ablation of stainless steel at high repetition rates, Opt. Express 22 (2014) 12200. https://doi.org/10.1364/OE.22.012200.
[15] E. Allahyari, J. Jj Nivas, E. Skoulas, R. Bruzzese, G.D. Tsibidis, E. Stratakis, S. Amoruso, On the formation and features of the supra-wavelength grooves generated during femtosecond laser surface structuring of silicon, Appl. Surf. Sci. 528 (2020) 146607. https://doi.org/10.1016/j.apsusc.2020.146607.
[16] F. Nyenhuis, P.N. Terekhin, T. Menold, B. Rethfeld, A. Michalowski, J.A. L'huillier, Fundamentals of Scanning Surface Structuring by Ultrashort Laser Pulses: From Electron Diffusion to Final Morphology, Adv. Photonics Res. 3 (2022) 2200045. https://doi.org/10.1002/adpr.202200045.
[17] G.D. Tsibidis, C. Fotakis, E. Stratakis, From ripples to spikes: A hydrodynamical mechanism to interpret femtosecond laser-induced self-assembled structures, Phys. Rev. B 92 (2015) 041405. https://doi.org/10.1103/PhysRevB.92.041405.
[18] C.A. Zuhlke, T.P. Anderson, D.R. Alexander, Formation of multiscale surface structures on nickel via above surface growth and below surface growth mechanisms using femtosecond laser pulses, Opt. Express 21 (2013) 8460. https://doi.org/10.1364/OE.21.008460.
[19] D.-H. Kam, J. Kim, L. Song, J. Mazumder, Formation mechanism of micro-spikes on AISI 4340 steel with femtosecond laser pulses at near-threshold fluence, J. Micromechanics Microengineering 25 (2015) 045007. https://doi.org/10.1088/0960-1317/25/4/045007.
[20] J. Bonse, S. Gräf, Maxwell Meets Marangoni—A Review of Theories on Laser-Induced Periodic Surface Structures, Laser Photonics Rev. 14 (2020) 2000215. https://doi.org/10.1002/lpor.202000215.
[21] G. Kónya, Z.F. Kovács, Effects of machining parameters, coolant oil composition, and coatings on the output characteristics of turning of X5CrNi18-10 stainless steel, Wear 570 (2025) 205893. https://doi.org/10.1016/j.wear.2025.205893.
[22] Y. Bouraoui, P. Woizeschke, T. Radel, 2D-FFT-based classification script for laser induced self organized surface structures, (2026). https://doi.org/10.17632/x6b6y3hzcb.1.
[23] A. Sikora, S. Nourry, M. Faucon, B. Chassagne, R. Kling, G. Mincuzzi, Role of the intensity profile in femtosecond laser surface texturing: An experimental study, Appl. Surf. Sci. Adv. 6 (2021) 100136. https://doi.org/10.1016/j.apsadv.2021.100136.
[24] S.V. Kirner, U. Hermens, A. Mimidis, E. Skoulas, C. Florian, F. Hischen, C. Plamadeala, W. Baumgartner, K. Winands, H. Mescheder, J. Krüger, J. Solis, J. Siegel, E. Stratakis, J. Bonse, Mimicking bug-like surface structures and their fluid transport produced by ultrashort laser pulse irradiation of steel, Appl. Phys. A 123 (2017) 754. https://doi.org/10.1007/s00339-017-1317-3.
[25] C. Florian Baron, A. Mimidis, D. Puerto, E. Skoulas, E. Stratakis, J. Solis, J. Siegel, Biomimetic surface structures in steel fabricated with femtosecond laser pulses: influence of laser rescanning on morphology and wettability, Beilstein J. Nanotechnol. 9 (2018) 2802–2812. https://doi.org/10.3762/bjnano.9.262.

[26] J. Bonse, S.V. Kirner, J. Krüger, Laser-Induced Periodic Surface Structures (LIPSS), in: K. Sugioka (Ed.), Handb. Laser Micro- Nano-Eng., Springer International Publishing, Cham, 2021: pp. 1–59. https://doi.org/10.1007/978-3-319-69537-2_17-2.
[27] C. Florian, R. Wonneberger, A. Undisz, S.V. Kirner, K. Wasmuth, D. Spaltmann, J. Krüger, J. Bonse, Chemical effects during the formation of various types of femtosecond laser-generated surface structures on titanium alloy, Appl. Phys. A 126 (2020) 266. https://doi.org/10.1007/s00339-020-3434-7.
[28] K.M.T. Ahmmed, E.J.Y. Ling, P. Servio, A.-M. Kietzig, Introducing a new optimization tool for femtosecond laser-induced surface texturing on titanium, stainless steel, aluminum and copper, Opt. Lasers Eng. 66 (2015) 258–268. https://doi.org/10.1016/j.optlaseng.2014.09.017.
[29] J.-T. Zhu, Y.-F. Shen, W. Li, X. Chen, G. Yin, D.-Y. Chen, L. Zhao, Effect of polarization on femtosecond laser pulses structuring silicon surface, Appl. Surf. Sci. 252 (2006) 2752–2756. https://doi.org/10.1016/j.apsusc.2005.04.048.
[30] G. Schnell, S. Bartling, R. Thomas, S.P. Nguyen, T. Block, S. Wolter, S. Lochbrunner, H. Seitz, Effect of the pulse repetition rate on the scalability of the ultrashort pulse laser process for generating laser-induced self-organized nano- and microstructures on stainless steel, Appl. Surf. Sci. Adv. 34 (2026) 101040. https://doi.org/10.1016/j.apsadv.2026.101040.
[31] G. Gomez-Munoz, R. Benítez-Fernández, G. Godoy-Perez, F. Cabello, M. Garcia-Pardo, D. Caudevilla, J. Gonzalo, J. Solis, M. Garcia-Lechuga, J. Olea, D. Pastor, J. Siegel, Tuning spike-like morphologies in Silicon by sustainable fs-laser processing in air for enhanced light absorption, Appl. Surf. Sci. 686 (2025) 161967. https://doi.org/10.1016/j.apsusc.2024.161967.
[32] J. Jj Nivas, S. He, A. Rubano, A. Vecchione, D. Paparo, L. Marrucci, R. Bruzzese, S. Amoruso, Direct Femtosecond Laser Surface Structuring with Optical Vortex Beams Generated by a q-plate, Sci. Rep. 5 (2015) 17929. https://doi.org/10.1038/srep17929.
[33] E.J.Y. Ling, J. Saïd, N. Brodusch, R. Gauvin, P. Servio, A.-M. Kietzig, Investigating and understanding the effects of multiple femtosecond laser scans on the surface topography of stainless steel 304 and titanium, Appl. Surf. Sci. 353 (2015) 512–521. https://doi.org/10.1016/j.apsusc.2015.06.137.